



Photocurrent Enhancement of PtSe₂ Photodetectors by Using Au Nanorods

Tatsuya Nakazawa ^{1,2} , Donghyun Kim ¹, Shinichi Kato ^{3,4}, Jusang Park ¹ , Jwamin Nam ³ and Hyungjun Kim ^{1,*}

¹ School of Electrical and Electronic Engineering, Yonsei University, 262 Seongsanno, Seodaemun-gu, Seoul 03722, Korea; t-nakazawa@yonsei.ac.kr (T.N.); kdh9319@yonsei.ac.kr (D.K.); jusang@yonsei.ac.kr (J.P.)

² Tanaka Kikinzoku Kogyo K.K. Isehara Technical Center, Metallic Materials Development Department, 28 Suzukawa, Isehara 259-1146, Kanagawa, Japan

³ Department of Chemistry, Seoul National University, 1 Gwanak-ro, Gwanak-gu, Seoul 08826, Korea; 2019-20165@snu.ac.kr (S.K.); jmnam@snu.ac.kr (J.N.)

⁴ Tanaka Kikinzoku Kogyo K.K. Hiratsuka Technical Center, Biochemical Development Department, 2-73 Shinmachi, Hiratsuka 254-0076, Kanagawa, Japan

* Correspondence: hyungjun@yonsei.ac.kr

Abstract: Compact and highly sensitive near-infrared photodetectors that are operable at room temperature are required for light detection and ranging and medical devices. Two-dimensional (2D) PtSe₂, a transition metal dichalcogenide, is a candidate material for near-infrared light detection. However, the photoresponse properties of 2D PtSe₂ are currently inferior to those of commercial materials. The localized surface plasmon resonance of Au has been widely used for photoelectric field enhancement and in photochemical reactions associated with phase relaxation from plasmon states that occur at specific wavelengths. Spherical Au nanocolloids exhibit an extinction peak in the visible light region, whereas nanorods can be tuned to exhibit the extinction peak in the near-infrared region by controlling their aspect ratio. In this study, hybrid Au nanorod/2D PtSe₂ structure was fabricated via spin coating nanorods, with plasmon peaks in the near-infrared region, on 2D PtSe₂. Furthermore, the effect of the concentration of the nanorod solution on the photoresponse of nanorod/2D PtSe₂ was investigated. The photocurrent of 5 nM Au nanorod-coated 2D PtSe₂ was fivefold higher than that of bare 2D PtSe₂. The responsivity was maximum 908 μW/A at 0.5 V bias voltage. In addition, the photocurrent enhancement mechanism by Au nanorods is discussed.

Keywords: 2D PtSe₂; Au nanorods; photodetector; localized surface plasmon resonance



Citation: Nakazawa, T.; Kim, D.; Kato, S.; Park, J.; Nam, J.; Kim, H. Photocurrent Enhancement of PtSe₂ Photodetectors by Using Au Nanorods. *Photonics* **2021**, *8*, 505. <https://doi.org/10.3390/photonics8110505>

Received: 19 October 2021

Accepted: 8 November 2021

Published: 10 November 2021

Publisher's Note: MDPI stays neutral with regard to jurisdictional claims in published maps and institutional affiliations.



Copyright: © 2021 by the authors. Licensee MDPI, Basel, Switzerland. This article is an open access article distributed under the terms and conditions of the Creative Commons Attribution (CC BY) license (<https://creativecommons.org/licenses/by/4.0/>).

1. Introduction

There is an increasing demand for near-infrared-light-detecting materials that can be operated at room temperature, for use in medical devices, analyzers, and light detection and ranging (LiDAR) [1,2]. LiDAR has applications in biometric authentication systems and augmented reality for electronic devices such as smartphones, which utilize a wavelength of 950 nm installed in camera units. Therefore, developing a light-detecting material that is compact and inexpensive and demonstrates high performance upon mounting on smart devices is essential.

InGaAs and HgCdTe have been proposed as potential light-receiving materials for LiDAR. However, HgCdTe is affected by low-temperature operation and contains toxic elements, also InGaAs requires a significantly expensive production process; therefore, alternative materials are desired [3–11]. In contrast, two-dimensional transition metal dichalcogenides (2D TMDCs), which have attracted attention as light-detecting materials in recent years, are chemically and physically stable and possess excellent optical and electrical properties [12]. MoS₂, MoSe₂, WS₂, and WSe₂ are well-known 2D TMDC materials that have been studied for their utilization as photodetector materials [13–16]. However, these 2D TMDCs possess wide bandgaps that are incompatible with the near-infrared

region; thus, their performance in the near-infrared region is limited [17]. Recently, PtSe₂ and PtS₂ have been proposed as 2D TMDC photodetection materials for application in the near-infrared region, as required for LiDAR [18]. In particular, 2D PtSe₂ has been reported to have a band gap that changes from 1.2 eV for a single layer to 0.33 eV for 17 layers [19,20]. 2D PtSe₂ and PtS₂ have suitable bandgaps for infrared detection and high mobility; therefore, 2D they are promising materials for use in near-infrared photodetectors. In addition, 2D PtSe₂ and PtS₂ photodetectors can be operated at room temperature and are thin and flexible owing to the characteristics of the 2D materials. Therefore, 2D PtSe₂ and PtS₂ are especially suitable materials for LiDAR applications in smartphones because of the demand for downsizing and lighter system units. Photodetector devices based on 2D PtSe₂ have been fabricated in previous studies, and they have exhibited photoresponse to near-infrared light [21]. However, the photoresponse properties of 2D PtSe₂ is currently inferior to those of commercial materials such as HgCdTe, and various methods to have been investigated for enhancing the photoresponse properties, such as the fabrication of heterojunctions [22,23].

Research on the enhancement of sensing properties has attracted considerable attention. A significant improvement was reported in the photoresponse of 2D TMDCs upon modifying their base materials. For example, the photoresponse can be enhanced by fabricating heterostructures, decorating the material with quantum dots, catalytic particle modifications, or using plasmonic materials [24,25]. Among them, achieving localized surface plasmon resonance (LSPR) using plasmonic materials is simple and is expected to be highly effective for photodetectors. Au colloids or nanoparticles, which possess a small imaginary part of permittivity, are typically used for LSPR [26,27]. Generally, spherical Au exhibits LSPR peaks in the visible light region [28,29]. Recently, research has been conducted to control the shape of particles and obtain spikes, rods, and heteromorphous nanoparticles that can achieve localized surface plasmon effects at wavelengths different from those of spherical nanoparticles [30,31]. In particular, it is possible to use nanorods to obtain a localized surface plasmon effect at the desired wavelength because their absorption peak can be controlled by changing the aspect ratio [32]. The longitudinal plasmon wavelength of Au nanorods has a high linear dependence on the length-to-diameter aspect ratio; minor changes in their aspect ratio have a significant impact on their optical properties [25,33–36]. Therefore, it is a common practice to isolate and purify Au nanorods after their synthesis to obtain the desired rod shape.

In this study, we fabricated 2D PtSe₂, which is a promising light-detecting material in the near-infrared region, via a one-step synthesis process involving chemical vapor deposition (CVD). Subsequently, synthesized Au nanorods, which exhibited an LSPR peak in the near-infrared region, were coated on 2D PtSe₂. The photoresponse properties of the obtained Au nanorods/2D PtSe₂ were investigated for various applications, such as the smartphone LiDAR system. Furthermore, the relationship between the surface coverage of the nanorods and the photocurrent was investigated, and the enhanced photocurrent mechanism is discussed. In addition, the effect of the precise purification of the Au nanorods on the photoresponse was studied.

2. Materials and Methods

Hydroquinone (HQ), 99%, hydrogen tetrachloroaurate trihydrate (HAuCl₄·3H₂O), ≥99.9%, silver nitrate (AgNO₃), ≥9%, benzyltrimethylammonium chloride (BDAC), ≥95%, and cetyltrimethylammonium bromide (CTAB), ≥99%, were purchased from Sigma-Aldrich, St. Louis, USA. Sodium borohydride (NaBH₄), chemically pure, was obtained from DaeJung Chemicals & Metals Co., Ltd., Siheung-si, Republic of Korea. Aqueous solutions of HQ and NaBH₄ were prepared freshly each day in the laboratory. All chemicals were used without further purification. Deionized water (DIW) which has electrical resistance greater than 18.0 MΩ was prepared by Milli-Q (Merck, Darmstadt, Germany).

Au nanorods were synthesized using a previously, reported method with slight modifications [37]. First, Au nanorod seeds were prepared according to the following

steps: 0.5 mL of 100 mM CTAB and 0.5 mL of 1 mM HAuCl_4 solution were mixed well. To this solution, 60 μL of 10 mM NaBH_4 solution dissolved in ice-chilled water was quickly added, and the mixture was vortexed for 2 min, resulting in a change in color from clear to pale brown. This solution was stored at 30 °C until it was used in the subsequent growth reaction. To a mixture of CTAB (5 mL, 200 mM) and HAuCl_4 (5 nL, 1 mM), 70 μL of 100 mM AgNO_3 solution was added, followed by 500 μL of 100 mM HQ. The resulting mixture was stirred until the color of the solution changed from yellow to colorless. Subsequently, 320 μL of the seed solution was added, and the growth solution was mixed thoroughly and incubated overnight at 30 °C for the growth of particles. The synthesized Au nanorods were centrifuged twice at $12,000\times g$ for 10 min in DIW and then redispersed for further purification. The as-synthesized nanorod solution contained spherical and cubic particles as by-products. To separate these from the rods, selective refinement was performed via a depletion-induced flocculation method [38]. BDAC and CTAB stock solutions were added to 500 μL of crude nanorod solution, along with DIW, to achieve final concentrations of 300 and 1 mM of BDAC and CTAB, respectively, in the solution. After overnight incubation at 30 °C, the supernatant was carefully removed by a micropipette. The precipitate containing pure nanorods was redispersed in DIW and centrifuged twice. The purified Au nanorod solution was adjusted to final concentrations of 0.5, 1, 5, 10, 25, and 50 nM using DIW.

Images of Au nanorods were obtained via energy-filtering transmission electron microscopy (EFTEM, LIBRA 120, Carl Zeiss AG, Jena, Germany), and the image analysis was performed using ImageJ [39–41]. LSPR peaks were measured using a UV-vis spectrophotometer (HP 8453, Agilent Technologies, Inc., Santa Clara, CA, USA).

A 2D PtSe_2 film was prepared via CVD. The laboratory-made CVD equipment comprised a tube-type resistance-heating furnace as the chamber, a mass flow controller (MFC), and a vacuum pump (Figure S1a). Dimethyl (*N,N*-dimethyl-3-butene-1-amine-*N*) platinum (DDAP purity > 99%: Tanaka Kikinzoku Kogyo K.K., Tokyo, Japan) and Se powder (99.99% purity, Sigma-Aldrich, St. Louis, MO, USA) were used as the precursor and reactant, respectively. DDAP was heated to 67 °C and carried to the chamber along with 10 sccm of Ar gas. The Se powder was placed on an alumina boat and installed it upstream of the gas flow in the electric furnace. The Se powder was heated to 220 °C using a heating tape. Ar gas (100 sccm) was flowed in the chamber. The MFC was used to control all gas flows. The furnace temperature was set to 400 °C, and the processing time was 15 min. A layered 2D PtSe_2 film was directly deposited on an -OH-terminated SiO_2/Si substrate. The Au nanorod solution (100 μL) was spin coated onto the 2D PtSe_2 film at 2000 rpm for 30 s.

The surface morphology of the film was studied via field emission scanning electron microscopy (FE-SEM, JSM-7610F-Plus, JEOL Ltd., Tokyo, Japan), and the image analysis was performed using ImageJ [39–41]. The SEM image is binarized to distinguish between nanorods and PtSe_2 . The nanorod coverage is then calculated by measuring the area of the nanorods relative to the total image area. A plugin for the analysis of porous scaffolds was used to measure the rod-to-rod distance [42]. Raman spectroscopy was performed using a LabRAM ARAMIS with 532 nm-wavelength laser (HORIBA, Kyoto, Japan) Raman microscope. Mobility was measured using a Hall effect measurement system (HMS3000, Ecopia Corporation, Anyang-si, Republic of Korea) with a 0.51 T magnetic field and a 0.1 μA current. The film thickness was measured by atomic force microscopy (AFM, NanoScope IIIa, Digital Instruments, Bresso, Italy). Data for the absorption curves were collected from an ultraviolet-visible-NIR (UV-Vis-NIR) spectrometer (V-670, JASCO Corporation, Tokyo, Japan). Further, sheet resistance was measured using a probe station with a four-point probe unit (M4P 205-System, MS TECH, Suwon-si, Korea).

LEDs (wavelength: 940 nm) were used as the light source for the photoresponse measurement. The power density of the LED lights mounted on a universal board was $525 \mu\text{W}/\text{cm}^2$. The universal board was ON/OFF-programmed to work with the light on for 20 s and off for 30 s. The photoresponse was measured using a voltage/current meter (Keithley 2400, Tektronix, Inc. Keithley Instruments, Solon, OH, USA) with a bias voltage of 0.5 V. The device was connected with alligator clips, and pressed indium grains were

used as contacts. Short duration precise photocurrent was measured using a probe station (M4P 205-System, MS TECH, Suwon-si, Korea).

3. Results & Discussion

Au nanorods were synthesized from a HAuCl_4 solution (Sigma-Aldrich, St. Louis, MO, USA). CTAB (Sigma-Aldrich, St. Louis, MO, USA) was used as a protectant, and it formed a layer of 2.0 nm thickness around the Au nanorods. For the synthesis, 5.9 is the desired aspect ratio to obtain the plasmon extinction peak at 940 nm. The Au nanorods were dispersed in water and adjusted to an arbitrary concentration. The EFTEM images show that the nanorods possessed a uniform rod shape (Figure 1a). The color depth of Au nanorods is caused by the different growth directions of the faceted Au nanorods, and the size and thickness are uniformly controlled [43]. The average size of the Au nanorods was calculated by image analysis to be $97.5 \text{ nm} \times 16.9 \text{ nm}$ ($n = 200$) (Figure 1b). Absorption spectra were collected using a UV-Vis-NIR spectrophotometer, and the position of the extinction peak was compared with that obtained using a spectral simulation method that used a quasi-electrostatic field approximation for a spheroid. The long-axis plasmon extinction peak at 940 nm and the short-axis peak at approximately 500 nm are in good agreement with those of the spectrum obtained via simulation (Figure 1c).

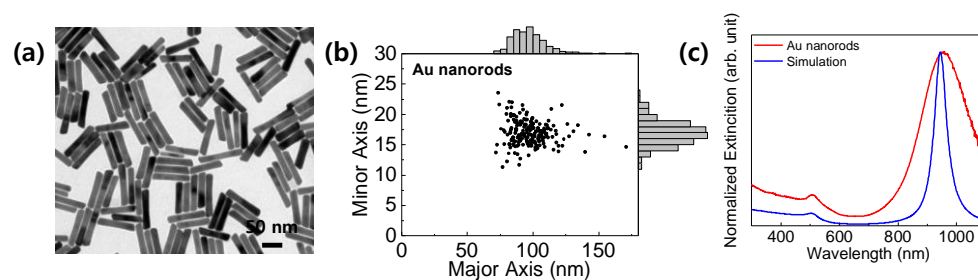


Figure 1. (a) TEM image of Au nanorods and (b) size distribution of purified Au nanorods. (c) Comparison of the extinction spectrum of purified Au nanorods and that obtained via simulation.

2D PtSe_2 was prepared via CVD to control the number of layers and surface roughness. In the CVD process, DDAP (Tanaka Kikinzoku Kogyo K.K., Tokyo, Japan) and vaporized Se were used as the precursor and reactant, respectively (Figure S1b). The synthesized PtSe_2 was confirmed to have a layered 2D structure via Raman spectroscopy, with the A_{1g} (out-of-plane vibration) and E_g (in-plane vibration) peaks at 208.5 and 180 cm^{-1} , respectively (Figure S1c) [44,45]. The 2D PtSe_2 indicated $2.67 \text{ cm}^2/\text{Vs}$ mobility, which is lower than reported value due to a fine structure with a lot of grain boundaries [46,47]. The thickness of the 2D PtSe_2 was 4.08 nm and the optical band gap was 0.88 eV , which are in agreement with the values reported in the literature for four layer PtSe_2 (Figure S1d,e) [20,48]. Then, samples with different concentrations of Au nanorods (0.5, 1, 5, 10, 25, and 50 nM) were used to determine the optimal amount of Au nanorods on the 2D PtSe_2 surface (Figure S2). Au nanorods were decorated on 2D PtSe_2 by spin coating at 2000 rpm to obtain Au nanorod/ 2D PtSe_2 hybrid structures. Au nanorods on 2D PtSe_2 were observed via FE-SEM. The Au nanorods (1–50 nM) were uniformly and randomly coated on 2D PtSe_2 ; however, almost no Au nanorods were observed on the 2D PtSe_2 surface with 0.5 nM Au nanorods (Figure 2a–e). The Au nanorod coverage on 2D PtSe_2 for each concentration of the Au nanorod solution was calculated by image analysis. The coverage of Au nanorods on 2D PtSe_2 is almost proportional to the concentration of the Au nanorod solution (Figure 2f). The Raman spectra after spin coating of Au nanorods show an increase in the A_{1g} peak compared to before coating (Figure S1c). It has been reported that the A_{1g} mode is strongly coupled with electrons in the functionalized 2D TMDCs by nanoparticles [49,50]. The increase in the A_{1g} peak suggests that the decoration of the Au nanorods affected the electron state in 2D PtSe_2 .

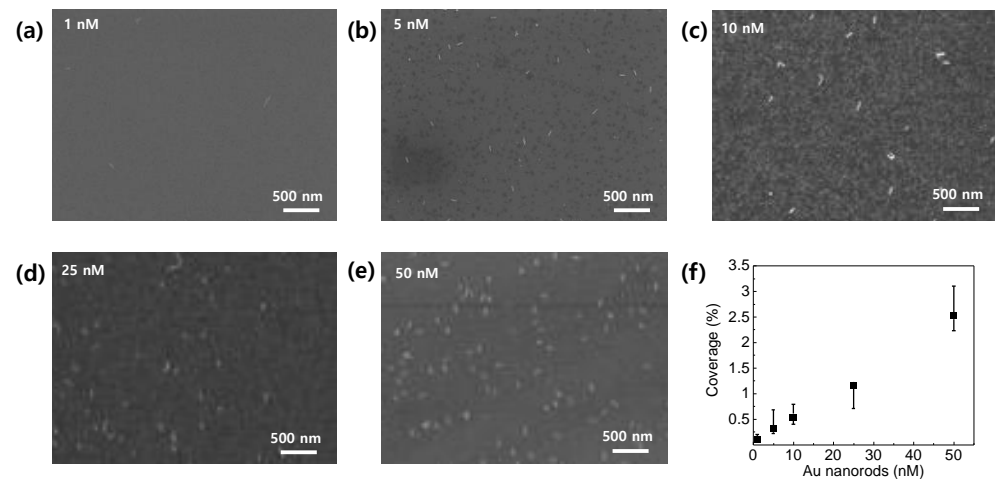


Figure 2. SEM image of 2D PtSe₂ surface coated by (a) 1, (b) 5, (c) 10, (d) 25, and (e) 50 nM Au nanorods. (f) Relationship between the concentration of Au nanorod solution and coverage.

A photoresponse-sensing electrode on Au nanorod/2D PtSe₂ substrate was fabricated by the thermal evaporation and deposition of Ti as the adhesion layer (thickness: 5 nm) and Au as the electrode (thickness: 40 nm), using an interdigitated comb shadow mask (Figures 3a and S3). Furthermore, a bare 2D PtSe₂ electrode was fabricated using the same method, to compare the photocurrent. For measuring the photocurrent, the electrodes were clamped using alligator clips connected to a multimeter. Using the multimeter, 0.5 V bias voltage was applied to the devices during the photocurrent measurement. The time-dependent photoresponse of the Au nanorod/2D PtSe₂ hybrid-structure photodetector was measured using LED light with a wavelength of 940 nm.

The photocurrent was observed in all samples and the dark current increased with higher concentration of Au nanorods (Figure 3b,c) [51]. As already reported, significantly faster photocurrent response times of 2D PtSe₂ compared to other 2D materials were observed [52]. The photocurrent increased in the photodetectors of up to 5 nM Au nanorod-coated 2D PtSe₂. The power dependence of photocurrent, responsivity, and ON/OFF cyclic performance test of 5 nM Au nanorod-coated 2D PtSe₂, which observed the highest photocurrent, were measured (Figures 3d,e and S4). It has been reported that the responsivity of PtSe₂ on SiO₂/Si substrate is 0.8 mA/W at 4.5 V bias voltage [53]. The responsivity measured in this study was maximum 908 μ W/A at 0.5 V bias voltage. Considering the difference in bias voltage, sufficient quality Au nanorod/2D PtSe₂ photodetectors were fabricated. The photocurrent in 5 nM Au-nanorod-coated 2D PtSe₂ is approximately fivefold higher than that in bare 2D PtSe₂. The increase in photocurrent of Au nanorod/2D PtSe₂ is remarkable and superior to that of functionalized TMDCs with metal nanoparticles [54–56]. However, the photocurrent decreased in 2D PtSe₂ decorated with Au nanorods of concentrations higher than 10 nM. Many papers have reported an enhancement in the properties of semiconductor materials by modifying the LSPR using plasmonic nanoparticles [57–63]. The photocurrent enhancement occurred because of the injection of hot electrons into the semiconductor material; these electrons were generated in the charge-separated state during specific radiative decay, such as Landau decay, from the plasmon state [64,65]. Consequently, the carrier concentration in the semiconductor increased, and the properties of the semiconductor material were improved [57].

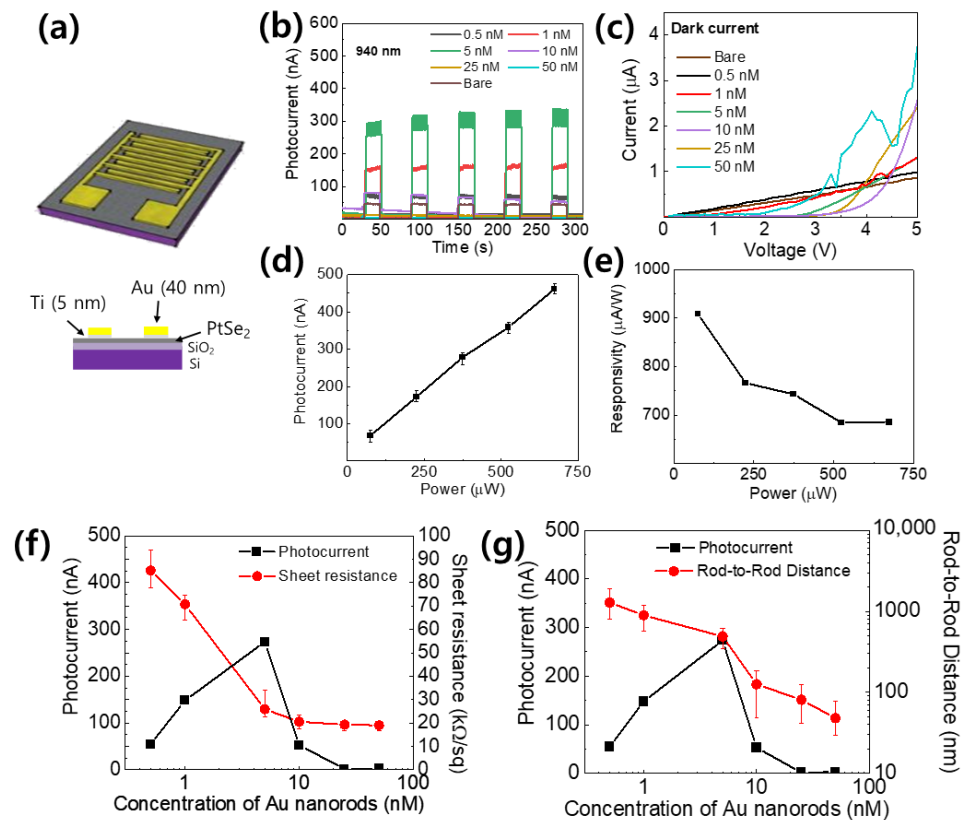


Figure 3. (a) Schematic of a comb-structure electrode. (b) Time-dependent photoresponse of Au nanorods of each concentration/2D PtSe₂ at 940 nm. (c) Dark current of each concentration of Au nanorod/2D PtSe₂. (d) Power dependence of photocurrent from 5 nM Au nanorod/2D PtSe₂. (e) Responsivity of 5 nM Au nanorod/2D PtSe₂. (f) Relationship between concentration of the Au nanorod solution and sheet resistance of Au nanorod/2D PtSe₂. (g) Relationship between concentration of the Au nanorod solution and rod-to-rod distance.

Previous studies on the decoration of semiconductors with Au nanoparticles have found that increasing the load of nanoparticles often causes performance degradation. These studies have proposed various explanations for the performance degradation. For example, Lee et al. proposed that Au nanorods act as light-shielding metal masks; thus, increasing the coverage of the Au nanorods decreases the quantum efficiency of 2D PtSe₂ [58,66]. However, in this case, although the surface coverage of the Au nanorods was only 0.5% with a 10 nM Au nanorod coating, the photocurrent decreased. Even 50 nM Au nanorod-coated 2D PtSe₂, which demonstrated only 1/20 of the photocurrent of bare 2D PtSe₂, possessed an Au nanorod coverage of 2.52%. Therefore, the photocurrent was measured by covering 3% of the device with a light-shielding tape to check the masking effect. The photocurrent of the 3%-covered device was almost equal to that of the bare 2D PtSe₂ (Figure S5). Therefore, 3% shielding did not cause a significant decrease in the photocurrent.

Metal nanoparticles decorated on semiconductors may also behave as recombination centers and cause exciton quenching [67–69]. However, our synthesized Au nanorods were capped by CTAB. CTAB surrounds the nanorods by a few nm and acts as a protectant. Generally, the thickness of the CTAB layer in solution is about 3 nm. However, on the surface of dried nanoparticles coated on a substrate, the CTAB layer becomes much thicker [70]. Studies of core–shell particles suggest that a thickness of 7–10 nm is necessary to act like a dielectric layer, and the thickness of the CTAB layer on the substrate is considered to be approximately the same [71]. CTAB layer avoids direct metal–semiconductor contact and prevents the Au nanorods from acting as recombination centers, thus preventing exciton quenching.

The other mechanism proposed for the decreasing photocurrent at high catalytic performance of TiO₂ and g-C₃N₄ catalysts decorated with Au nanoparticles is the enhancement of electron–hole recombination owing to leakage current caused by excess hot electrons under high Au loading [59–62]. Furthermore, measurements of sheet resistance showed that the leakage current increases with an increase in the Au nanoparticle loading. It is considered that the formation of false transport channels by Au nanoparticles results in the loss of carriers [63]. Au nanorod solutions of various concentrations were coated on 2D PtSe₂ films, and the sheet resistances were measured. The sheet resistance decreased with an increase in the concentration of Au nanorods (Figure 3f). Notably, in the 10 nM Au-nanorod-decorated sample, which exhibited a lower photocurrent than those of samples coated with lower concentrations of Au nanorod solution, the sheet resistance was as low as those of the 25 and 50 nM solution-coated samples that exhibited a significantly degraded photocurrent.

Moreover, the theoretical mean free path of hot electrons in metals is 10–60 nm [72]. By measuring the distances between the nanorods from the FE-SEM images, we found that the photocurrent decreased in devices with regions where the distance between the nanorods was less than 60 nm (Figure 3g). Therefore, the leakage current owing to the hot-electron mean free path is responsible for the decrease in the photocurrent. Thus, the formation of excessive false transport channels can be avoided by maintaining a distance greater than the mean free path of hot electrons (10–60 nm) between the Au nanorods.

In addition, the electric field around the Au nanorods was simulated by pyGDM to discuss the effect of electric field enhancement by LSPR [73]. The simulation results show that the electric field is enhanced in a region of about 50 nm around the nanorods (Figure 4a). Calculations were also performed for two Au nanorods with a 10 nm gap to simulate the electric field for high concentration nanorods are coated, and a 60 nm gap to compare. The calculation results for a 60 nm gap indicated a slightly blue-shifted extinction peak, while a 10 nm gap indicated a significant peak blue-shifted to approximately 850 nm due to plasmon hybridization (Figure 4b–d) [74]. Therefore, from the viewpoint of electric field enhancement, it was indicated that a rod-to-rod distance of more than 60 nm was effective in enhancing the photocurrent.

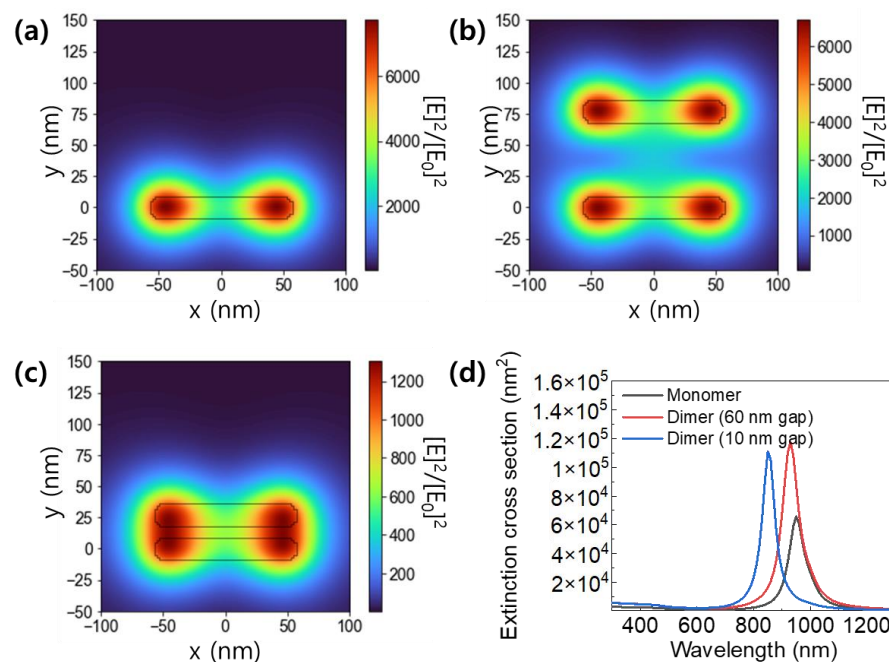


Figure 4. Electric field simulation via pyGDM for (a) a single Au nanorod, (b) two Au nanorods with 60 nm spacing, and (c) two Au nanorods with 10 nm spacing. (d) Comparison of the simulated extinction spectrum of each nanorod placement.

Nanoparticles with undesired shapes were produced during the synthesis of Au nanorods. Therefore, the separation and purification of the desired nanorods is a common procedure before using the nanorods. An unpurified (as-synthesized) Au nanorod solution (5 nM) was prepared to investigate the significance of purification in enhancing the photocurrent of the nanorods. From the EFTEM images, 71% of the particles were Au particles with the desired rod shape. The imperfectly shaped Au nanocolloids contained spherical and cube-shaped lumps and nanorods with insufficient longitudinal growth (Figure 5a). The size distribution of Au nanorods was broader than after purification (Figure 5b). Absorption spectra were recorded using a UV-vis-NIR spectrophotometer, and the long-axis plasmon extinction peak at 940 nm and the short-axis peak at approximately 500 nm were almost the same as those of the purified Au nanorods (Figure 5c). However, the slightly higher intensity of the short-axis peaks around 500 nm of the as-synthesized sample compared with those of the purified Au nanorods could be because of the imperfectly shaped Au nanoparticles (Figure 5d). The short axis peak has a broad shoulder due to the long-axes of incomplete rods.

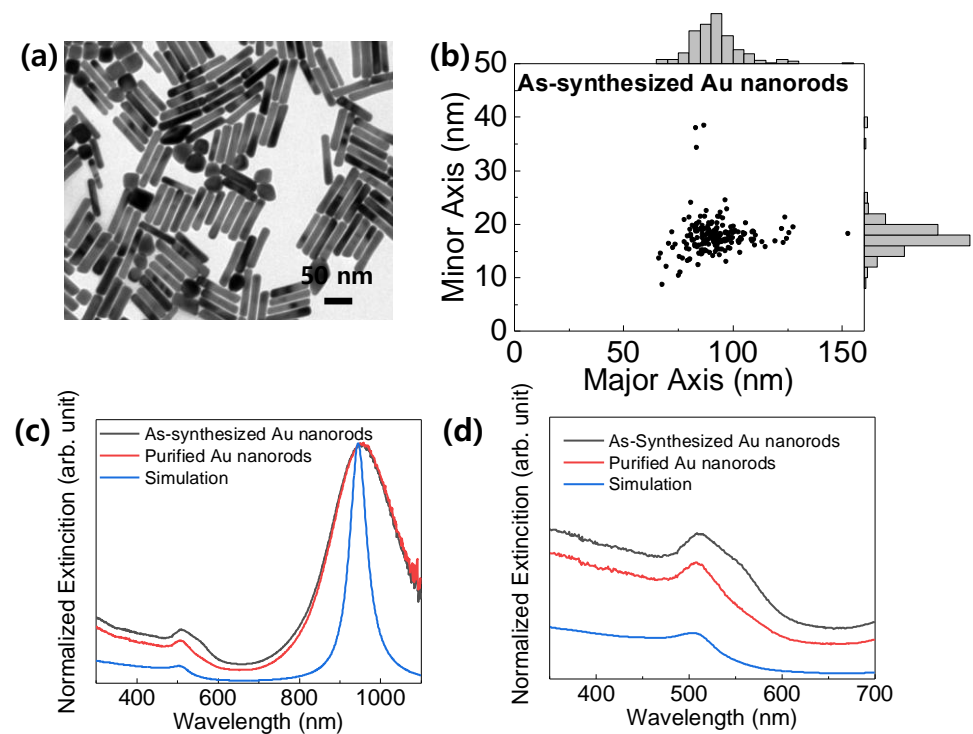


Figure 5. (a) TEM image of as-synthesized Au nanorods. (b) Size distribution of as-synthesized Au nanorods. (c) Extinction spectra of as-synthesized and purified Au nanorods and that obtained via simulation. (d) Extinction spectra of as-synthesized and purified Au nanorods and that obtained via simulation attributed as short-axis.

The as-synthesized Au nanorod solution (5 nM) was spin coated onto 2D PtSe₂ in the same way that purified Au nanorod solutions and Au/Ti interdigitated comb electrodes were fabricated on the surface to measure the photocurrent. A probe station was used to measure the precise photocurrent in a short time. The maximum photocurrent of the as-synthesized Au nanorod/2D PtSe₂ was almost the same as that of the generated Au nanorod/2D PtSe₂. As for the photocurrent response time, the 10–90% rise time of the as-synthesized Au nanorod/2D PtSe₂ was measured to be approximately 0.3 s, which was slightly slower than that of the purified Au nanorod/2D PtSe₂ and bare 2D PtSe₂ of approximately 0.2 s (Figure 6a–c). However, the as-synthesized Au nanorod/2D PtSe₂ showed a continual increase after the steep increase in photocurrent in a short time. Moreover, the photocurrent variation was large, and the standard deviation differed greatly, i.e., $\sigma_{As-synthesized} = 21.20$ nA and $\sigma_{Purified} = 4.23$ nA, while the bare 2D PtSe₂

was $\sigma_{Bare} = 0.40$ nA (Figure 6d–e). Theoretically, the injection efficiency of hot electrons varies with the shape of the Au nanoparticles [75]. The efficiency of hot-electron injection is less in low-aspect-ratio nanorods and spherical particles. Additionally, CTAB, which is used as a protectant for Au nanorods, is positively charged and can trap electrons unless sufficient hot electrons are generated in the Au nanorods [76]. The irregular/non-flat steps are presumed to be the result of the imperfectly shaped Au nanorods acting as electron traps as well as electron donors by generated hot electrons; hence, the photocurrent was not stably generated.

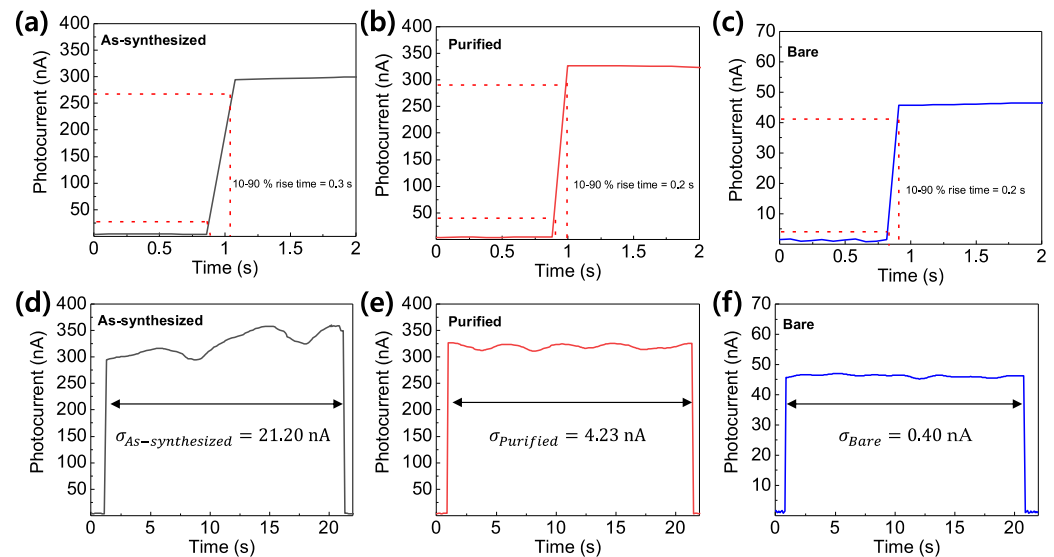


Figure 6. 10–90% rise time of (a) as-synthesized Au nanorod/2D PtSe₂, (b) purified Au nanorod/2D PtSe₂, and (c) bare 2D PtSe₂. Variation in photocurrent of (d) as-synthesized Au nanorod/2D PtSe₂, (e) purified Au nanorod/2D PtSe₂, and (f) bare 2D PtSe₂.

As mentioned above, imperfect nanorods in the Au nanorod solutions possessed low aspect ratios and were cube-shaped and spherical particles. Such nanorods did not generate sufficient hot-electron injection effect, resulting in unstable photocurrent generation due to electron trapping by the positively charged protectant CTAB. Therefore, the purification of nanorods has the effect of increasing the hot electron injection efficiency and generating a fast response and stable enhanced photocurrent at 940 nm.

4. Conclusions

In this study, 2D PtSe₂ was prepared via CVD using DDAP and Se as precursor and reactant, respectively. Au nanorods with an aspect ratio of 5.9, which exhibited an absorption peak at 940 nm, were synthesized to improve the photoresponse properties of 2D PtSe₂. The extinction spectra of the synthesized Au nanorods were in good agreement with the simulation results. Furthermore, the Au nanorod solution was diluted with pure water to prepare solutions of six different concentrations. These solutions were spin coated to obtain Au nanorod/2D PtSe₂ hybrid structures. Then, comb electrodes were fabricated using Au nanorod/2D PtSe₂ and their time-dependent photoresponse to near-infrared light (wavelength: 940 nm) was measured. A high photocurrent was observed in 2D PtSe₂ decorated with 5.0 nM Au nanorods, which was approximately fivefold higher than that of bare 2D PtSe₂. On the other hand, the photocurrent decreased with an increase in the Au nanorod concentration above 10 nM. The leakage current increased possibly owing to the formation of false transport channels because the spacing between the Au nanorods was less than the mean free path of the hot electrons. The standard deviation of photocurrent was larger with unpurified Au nanorod coating because of the imperfectly shaped Au nanoparticles in the Au nanorod solution. Therefore, refining the Au nanorods is important for stable enhancement of photocurrent. The photocurrent can be improved via a simple

method of spin coating the purified Au nanorods of appropriate concentrations onto 2D PtSe₂ films.

Supplementary Materials: The following are available online at <https://www.mdpi.com/article/10.3390/photonics8110505/s1>, Figure S1: (a) Schematic of the CVD process for the fabrication of 2D PtSe₂. (b) Structure of DDAP. (c) Raman spectrum of 2D PtSe₂ before and after Au nanorods spin coating. (d) AFM image of 2D PtSe₂. (e) Tauc plot of 2D PtSe₂ calculated from UV-vis-NIR spectra. Figure S2: Photograph of Au nanorod solutions of various concentrations. Figure S3: Dimensional drawing of the interdigitated comb shadow mask. Figure S4: ON/OFF cyclic performance test of 5 nM Au nanorod/2D PtSe₂ at 940 nm. Figure S5: Photocurrent comparison of 3% masked Au nanorod/2D PtSe₂ and bare 2D PtSe₂ at 940 nm.

Author Contributions: Conceptualization, T.N. and D.K.; methodology, T.N. and S.K.; LSPR peak simulation, S.K.; validation, D.K.; formal analysis, T.N.; investigation, T.N.; data curation, T.N., D.K., and S.K.; writing—original draft preparation, T.N.; writing—review and editing, J.P.; supervision, J.N. and H.K.; project administration, H.K. All authors have read and agreed to the published version of the manuscript.

Funding: This research was funded by Tanaka Kikinzoku Kogyo K.K. and National Research Foundation of Korea (NRF) grant funded by the Korea government (MSIT). (No. NRF-2021R1A2C3010083).

Institutional Review Board Statement: Not applicable.

Informed Consent Statement: Not applicable.

Conflicts of Interest: The authors declare no conflict of interest.

References

1. Rozlosnik, A. Potential Contribution of the Infrared Industry in the Future of IoT/IloT. In Proceedings of the 14th Quantitative Infrared Thermography Conference, Berlin, Germany, 25–29 June 2018; pp. 194–208. [\[CrossRef\]](#)
2. Chetan, N.B.; Gong, J.; Zhou, H.; Bi, D.; Lan, J.; Qie, L. An Overview of Recent Progress of Lane Detection for Autonomous Driving. In Proceedings of the 6th International Conference on Dependable Systems and Their Applications, Harbin, China, 3–6 January 2020; pp. 341–346. [\[CrossRef\]](#)
3. Maruyama, T.; Narusawa, F.; Kudo, M.; Tanaka, M.; Saito, Y.; Nomura, A. Development of a Near-Infrared Photon-Counting System Using an InGaAs Avalanche Photodiode. *Opt. Eng.* **2002**, *41*, 395. [\[CrossRef\]](#)
4. Bone, P.A.; Ripalda, J.M.; Bell, G.R.; Jones, T.S. Surface Reconstructions of InGaAs Alloys. *Surf. Sci.* **2006**, *600*, 973–982. [\[CrossRef\]](#)
5. Moazzami, K.; Phillips, J.; Lee, D.; Krishnamurthy, S.; Benoit, G.; Fink, Y.; Tiwald, T. Detailed Study of Above Bandgap Optical Absorption in HgCdTe. *J. Electron. Mater.* **2005**, *34*, 773–778. [\[CrossRef\]](#)
6. Arias, J.M.; Pasko, J.G.; Zandian, M.; Kozlowski, L.J.; DeWames, R.E. Molecular Beam Epitaxy HgCdTe Infrared Photovoltaic Detectors. *Opt. Eng.* **1994**, *33*, 1422. [\[CrossRef\]](#)
7. Kinch, M.A.; Borrello, S.R.; Simmons, A. 0.1 eV HgCdTe Photoconductive Detector Performance. *Infrared Phys.* **1977**, *17*, 127–135. [\[CrossRef\]](#)
8. Ashcroft, A.; Baker, I. Developments in HgCdTe Avalanche Photodiode Technology and Applications. In Proceedings of the SPIE Defense, Security, and Sensing, Orlando, FL, USA, 5–9 April 2010; Volume 7660, p. 76603C. [\[CrossRef\]](#)
9. Tchounwou, P.B.; Yedjou, C.G.; Patlolla, A.K.; Sutton, D.J. Heavy Metals Toxicity and the Environment Paul. *Mol. Clin. Environ. Toxicol.* **2012**, *101*, 133–164. [\[CrossRef\]](#)
10. Taylor, A. Biochemistry of Tellurium. *Biol. Trace Elem. Res.* **1996**, *55*, 231–239. [\[CrossRef\]](#)
11. European Commission Waste Electrical & Electronic Equipment Directive 2011/65/EU of the European Parliament and of the Council of 8 June 2011 on the restriction of the Use of Certain Hazardous Substances in Electrical and Electronic Equipment Text with EEA Relevance. *Off. J. Eur. Union* **2011**, *1*, 88–110.
12. Tang, W.; Rassay, S.; Ravindra, N. Electronic & Optical properties of transition-metal dichalcogenides. *Madridge J. Nanotechnol. Nanosci.* **2017**, *2*, 59–65. [\[CrossRef\]](#)
13. Xie, Y.; Zhang, B.; Wang, S.; Wang, D.; Wang, A.; Wang, Z.; Yu, H.; Zhang, H.; Chen, Y.; Zhao, M.; et al. Ultrabroadband MoS₂ Photodetector with Spectral Response from 445 to 2717 nm. *Adv. Mater.* **2017**, *29*. [\[CrossRef\]](#)
14. Chang, Y.H.; Zhang, W.; Zhu, Y.; Han, Y.; Pu, J.; Chang, J.K.; Hsu, W.T.; Huang, J.K.; Hsu, C.L.; Chiu, M.H.; et al. Monolayer MoSe₂ Grown by Chemical Vapor Deposition for Fast Photodetection. *ACS Nano* **2014**, *8*, 8582–8590. [\[CrossRef\]](#) [\[PubMed\]](#)
15. Tan, H.; Fan, Y.; Zhou, Y.; Chen, Q.; Xu, W.; Warner, J.H. Ultrathin 2D Photodetectors Utilizing Chemical Vapor Deposition Grown WS₂ with Graphene Electrodes. *ACS Nano* **2016**, *10*, 7866–7873. [\[CrossRef\]](#) [\[PubMed\]](#)
16. Zheng, Z.; Zhang, T.; Yao, J.; Zhang, Y.; Xu, J.; Yang, G. Flexible, Transparent and Ultra-Broadband Photodetector Based on Large-Area WSe₂ Film for Wearable Devices. *Nanotechnology* **2016**, *27*, 225501. [\[CrossRef\]](#) [\[PubMed\]](#)

17. Manzeli, S.; Ovchinnikov, D.; Pasquier, D.; Yazyev, O.V.; Kis, A. 2D Transition Metal Dichalcogenides. *Nat. Rev. Mater.* **2017**, *2*, 17033. [CrossRef]
18. Zhuang, H.L.; Hennig, R.G. Computational Search for Single-layer Transition-Metal Dichalcogenide Photocatalysts. *J. Phys. Chem. C* **2013**, *117*, 20440–20445. [CrossRef]
19. Wang, Y.; Li, L.; Yao, W.; Song, S.; Sun, J.T.; Pan, J.; Ren, X.; Li, C.; Okunishi, E.; Wang, Y.Q.; et al. Monolayer PtSe₂, a New Semiconducting Transition-Metal-Dichalcogenide, Epitaxially Grown by Direct Selenization of Pt. *Nano Lett.* **2015**, *15*, 4013–4018. [CrossRef]
20. Wang, L.; Zhang, S.; McEvoy, N.; Sun, Y.Y.; Huang, J.; Xie, Y.; Dong, N.; Zhang, X.; Kislyakov, I.M.; Nunzi, J.M.; et al. Nonlinear Optical Signatures of the Transition from Semiconductor to Semimetal in PtSe₂. *Laser Photonics Rev.* **2019**, *13*, 1900052. [CrossRef]
21. Yu, X.; Yu, P.; Wu, D.; Singh, B.; Zeng, Q.; Lin, H.; Zhou, W.; Lin, J.; Suenaga, K.; Liu, Z.; et al. Atomically Thin Noble Metal Dichalcogenide: A Broadband Mid-Infrared Semiconductor. *Nat. Commun.* **2018**, *9*, 1545. [CrossRef]
22. Wu, D.; Wang, Y.; Zeng, L.; Jia, C.; Wu, E.; Xu, T.; Shi, Z.; Tian, Y.; Li, X.; Tsang, Y.H. Design of 2D Layered PtSe₂ Heterojunction for the High-Performance, Room-Temperature, Broadband, Infrared Photodetector. *ACS Photonics* **2018**, *5*, 3820–3827. [CrossRef]
23. Li, L.; Wang, W.; Chai, Y.; Li, H.; Tian, M.; Zhai, T. Few-Layered PtS₂ Phototransistor on h-BN with High Gain. *Adv. Funct. Mater.* **2017**, *27*, 1701011. [CrossRef]
24. Kufer, D.; Nikitskiy, I.; Lasanta, T.; Navickaite, G.; Koppens, F.H.L.; Konstantatos, G. Hybrid 2D-0D MoS₂-PbS Quantum Dot Photodetectors. *Adv. Mater.* **2015**, *27*, 176–180. [CrossRef]
25. Chen, Y.T.; Hsieh, Y.P.; Shih, F.Y.; Chang, C.Y.; Hofmann, M.; Chen, Y.F. MOS Photodetectors Based on Au-Nanorod Doped Graphene Electrodes. *Nanotechnology* **2011**, *22*, 305201. [CrossRef] [PubMed]
26. Pockrand, I.; Raether, H. Surface Plasma Oscillations at Sinusoidal Silver Surfaces. *Appl. Opt.* **1977**, *16*, 1784–1786. [CrossRef]
27. Rycenga, M.; Cobley, C.M.; Zeng, J.; Li, W.; Moran, C.H.; Zhang, Q.; Qin, D.; Xia, Y. Controlling the Synthesis and Assembly of Silver Nanostructures for Plasmonic Applications. *Chem. Rev.* **2011**, *111*, 3669–3712. [CrossRef] [PubMed]
28. Esashika, K.; Ishii, R.; Tokihiro, S.; Saiki, T. Simple and Rapid Method for Homogeneous Dimer Formation of Gold Nanoparticles in a Bulk Suspension Based on van der Waals Interactions Between Alkyl Chains. *Opt. Mater. Express* **2019**, *9*, 1667. [CrossRef]
29. Jain, P.K.; Lee, K.S.; El-Sayed, I.H.; El-Sayed, M.A. Calculated Absorption and Scattering Properties of Gold Nanoparticles of Different Size, Shape, and Composition: Applications in Biological Imaging and Biomedicine. *J. Phys. Chem. B* **2006**, *110*, 7238–7248. [CrossRef]
30. Xie, J.; Lee, J.Y.; Wang, D.I.C. Seedless, Surfactantless, High-Yield Synthesis of Branched Gold Nanocrystals in HEPES Buffer Solution. *Chem. Mater.* **2007**, *19*, 2823–2830. [CrossRef]
31. Lohse, S.E.; Murphy, C.J. The Quest for Shape Control: A History of Gold Nanorod Synthesis. *Chem. Mater.* **2013**, *25*, 1250–1261. [CrossRef]
32. Xie, B.H.; Fei, G.T.; Xu, S.H.; Gao, X.D.; Zhang, J.X.; De Zhang, L. Tunable Broadband Wavelength-Selective Enhancement of Responsivity in Ordered Au-Nanorod Array-Modified PbS Photodetectors. *J. Mater. Chem. C* **2018**, *6*, 1767–1773. [CrossRef]
33. Pérez-Juste, J.; Pastoriza-Santos, I.; Liz-Marzán, L.M.; Mulvaney, P. Gold Nanorods: Synthesis, Characterization and Applications. *Coord. Chem. Rev.* **2005**, *249*, 1870–1901. [CrossRef]
34. Murphy, C.J.; Sau, T.K.; Gole, A.M.; Orendorff, C.J.; Gao, J.; Gou, L.; Hunyadi, S.E.; Li, T. Anisotropic Metal Nanoparticles: Synthesis, Assembly, and Optical Applications. *J. Phys. Chem. B* **2005**, *109*, 13857–13870. [CrossRef] [PubMed]
35. Liz-Marza, L.M. Tailoring Surface Plasmons through the Morphology and Assembly of Metal Nanoparticles. *Langmuir* **2006**, *22*, 32–41. [CrossRef] [PubMed]
36. Brioude, A.; Jiang, X.C.; Pileni, M.P. Optical Properties of Gold Nanorods: DDA Simulations Supported by Experiments. *J. Phys. Chem. B* **2005**, *109*, 13138–13142. [CrossRef] [PubMed]
37. Vigderman, L.; Zubarev, E.R. High-Yield Synthesis of Gold Nanorods with Longitudinal SPR Peak Greater than 1200 nm Using Hydroquinone as a Reducing Agent. *Chem. Mater.* **2013**, *25*, 1450–1457. [CrossRef]
38. Park, K.; Koerner, H.; Vaia, R.A. Depletion-Induced Shape and Size Selection of Gold Nanoparticles. *Nano Lett.* **2010**, *10*, 1433–1439. [CrossRef] [PubMed]
39. ImageJ Home Page. Available online: <https://imagej.nih.gov/ij/> (accessed on 5 May 2021).
40. Schneider, C.A.; Rasband, W.S.; Eliceiri, K.W. NIH Image to ImageJ: 25 Years of Image Analysis. *Nat. Methods* **2012**, *9*, 671–675. [CrossRef] [PubMed]
41. Abramoff, M.D.; Magalhães, P.J.; Ram, S.J. Image Processing with ImageJ. *Biophotonics Int.* **2004**, *11*, 36–41. [CrossRef]
42. Haeri, M.; Haeri, M. ImageJ Plugin for Analysis of Porous Scaffolds used in Tissue Engineering. *J. Open Res. Softw.* **2015**, *3*, 2–5. [CrossRef]
43. Wang, Z.L.; Mohamed, M.B.; Link, S.; El-Sayed, M.A. Crystallographic facets and shapes of gold nanorods of different aspect ratios. *Surf. Sci.* **1999**, *440*, L809–L814. [CrossRef]
44. Yan, M.; Wang, E.; Zhou, X.; Zhang, G.; Zhang, H.; Zhang, K.; Yao, W.; Lu, N.; Yang, S.; Wu, S.; et al. High Quality Atomically Thin PtSe₂ Films Grown by Molecular Beam Epitaxy. *2D Mater.* **2017**, *4*, 045015. [CrossRef]
45. Chen, X.; Zhang, S.; Wang, L.; Huang, Y.-F.; Liu, H.; Huang, J.; Dong, N.; Liu, W.; Kislyakov, I.M.; Nunzi, J.M.; et al. Direct Observation of Interlayer Coherent Acoustic Phonon Dynamics in Bilayer and Few-Layer PtSe₂. *Photonics Res.* **2019**, *7*, 1416. [CrossRef]

46. Sojková, M.; Dobročka, E.; Hutár, P.; Tašková, V.; Pribusová Slušná, L.; Stoklas, R.; Píš, I.; Bondino, F.; Munnik, F.; Hulman, M. High carrier mobility epitaxially aligned PtSe₂ films grown by one-zone selenization. *Appl. Surf. Sci.* **2021**, *538*, 147936. [[CrossRef](#)]
47. Zhao, Y.; Qiao, J.; Yu, Z.; Yu, P.; Xu, K.; Lau, S.P.; Zhou, W.; Liu, Z.; Wang, X.; Ji, W.; et al. High-Electron-Mobility and Air-Stable 2D Layered PtSe₂ FETs. *Adv. Mater.* **2017**, *29*, 1604230. [[CrossRef](#)]
48. Boland, C.S.; Coileáin, C.O.; Wagner, S.; McManus, J.B.; Cullen, C.P.; Lemme, M.C.; Duesberg, G.S.; McEvoy, N. PtSe₂ grown directly on polymer foil for use as a robust piezoresistive sensor. *2D Mater.* **2019**, *6*, 045029. [[CrossRef](#)]
49. Chakraborty, B.; Bera, A.; Muthu, D.V.S.; Bhowmick, S.; Waghmare, U.V.; Sood, A.K. Symmetry-dependent phonon renormalization in monolayer MoS₂ transistor. *Phys. Rev. B-Condens. Matter Mater. Phys.* **2012**, *85*, 2–5. [[CrossRef](#)]
50. Sohn, A.; Moon, H.; Kim, J.; Seo, M.; Min, K.A.; Lee, S.W.; Yoon, S.; Hong, S.; Kim, D.W. Band Alignment at Au/MoS₂ Contacts: Thickness Dependence of Exfoliated Flakes. *J. Phys. Chem. C* **2017**, *121*, 22517–22522. [[CrossRef](#)]
51. La, J.A.; Kang, J.H.; Byun, J.Y.; Kim, I.S.; Kang, G.; Ko, H. Highly sensitive and fast perovskite photodetector functionalized by plasmonic Au nanoparticles-alkanethiol assembly. *Appl. Surf. Sci.* **2021**, *538*, 148007. [[CrossRef](#)]
52. Zeng, L.H.; Lin, S.H.; Li, Z.J.; Zhang, Z.X.; Zhang, T.F.; Xie, C.; Mak, C.H.; Chai, Y.; Lau, S.P.; Luo, L.B.; et al. Fast, Self-Driven, Air-Stable, and Broadband Photodetector Based on Vertically Aligned PtSe₂/GaAs Heterojunction. *Adv. Funct. Mater.* **2018**, *28*, 1705970. [[CrossRef](#)]
53. Parhizkar, S.; Prechtel, M.; Giesecke, A.L.; Suckow, S.; Lukas, S.; Hartwig, O.; Quellmalz, A.; Gylfason, K.B.; Schall, D.; Duesberg, G.S.; et al. Waveguide-Integrated Photodetectors based on 2D Platinum Diselenide. In Proceedings of the 79th Device Research Conference (DRC), Virtual (online), 20–23 June 2021; pp. 1–2. [[CrossRef](#)]
54. Yin, Z.; Chen, B.; Bosman, M.; Cao, X.; Chen, J.; Zheng, B.; Zhang, H. Au nanoparticle-modified MoS₂ nanosheet-based photoelectrochemical cells for water splitting. *Small* **2014**, *10*, 3537–3543. [[CrossRef](#)]
55. Sriram, P.; Wen, Y.P.; Manikandan, A.; Hsu, K.C.; Tang, S.Y.; Hsu, B.W.; Chen, Y.Z.; Lin, H.W.; Jeng, H.T.; Chueh, Y.L.; et al. Enhancing Quantum Yield in Strained MoS₂ Bilayers by Morphology-Controlled Plasmonic Nanostructures toward Superior Photodetectors. *ACS Appl. Mater. Interfaces* **2020**, *32*, 2242–2252. [[CrossRef](#)]
56. Xu, X.; Luo, F.; Tang, W.; Hu, J.; Zeng, H.; Zhou, Y. Enriching Hot Electrons via NIR-Photon-Excited Plasmon in WS₂@Cu Hybrids for Full-Spectrum Solar Hydrogen Evolution. *Adv. Funct. Mater.* **2018**, *28*, 1804055. [[CrossRef](#)]
57. Hartland, G.V. Optical Studies of Dynamics in Noble Metal Nanostructures. *Chem. Rev.* **2011**, *111*, 3858–3887. [[CrossRef](#)]
58. Lee, K.C.J.; Chen, Y.H.; Lin, H.Y.; Cheng, C.C.; Chen, P.Y.; Wu, T.Y.; Shih, M.H.; Wei, K.H.; Li, L.J.; Chang, C.W. Plasmonic Gold Nanorods Coverage Influence on Enhancement of the Photoluminescence of Two-Dimensional MoS₂ Monolayer. *Sci. Rep.* **2015**, *5*, 16374. [[CrossRef](#)]
59. Yoshida, T.; Misu, Y.; Yamamoto, M.; Tanabe, T.; Kumagai, J.; Ogawa, S.; Yagi, S. Effects of the Amount of Au Nanoparticles on the Visible Light Response of TiO₂ Photocatalysts. *Catal. Today* **2020**, *352*, 34–38. [[CrossRef](#)]
60. Ding, D.; Liu, K.; He, S.; Gao, C.; Yin, Y. Ligand-Exchange Assisted Formation of Au/TiO₂ Schottky Contact for Visible-Light Photocatalysis. *Nano Lett.* **2014**, *14*, 6731–6736. [[CrossRef](#)]
61. Dai, Y.; Zhu, M.; Wang, X.; Wu, Y. Visible-light Promoted Catalytic Activity of Dumbbell-Like Au Nanorods Supported on Graphene/TiO₂ Sheets Towards Hydrogenation Reaction. *Nanotechnology* **2018**, *29*, 245703. [[CrossRef](#)]
62. Guo, Y.; Jia, H.; Yang, J.; Yin, H.; Yang, Z.; Wang, J.; Yang, B. Understanding the Roles of Plasmonic Au Nanocrystal Size, Shape, Aspect Ratio and Loading Amount in Au/g-C₃N₄ Hybrid Nanostructures for Photocatalytic Hydrogen Generation. *Phys. Chem. Chem. Phys.* **2018**, *20*, 22296–22307. [[CrossRef](#)]
63. Ho, Y.C.; Kao, S.H.; Lee, H.C.; Chang, S.K.; Lee, C.C.; Lin, C.F. Investigation of the Localized Surface Plasmon Effect from Au Nanoparticles in ZnO Nanorods for Enhancing the Performance of Polymer Solar Cells. *Nanoscale* **2015**, *7*, 776–783. [[CrossRef](#)] [[PubMed](#)]
64. Govorov, A.O.; Zhang, H.; Gun'ko, Y.K. Theory of Photoinjection of Hot Plasmonic Carriers from Metal Nanostructures into Semiconductors and Surface Molecules. *J. Phys. Chem. C* **2013**, *117*, 16616–16631. [[CrossRef](#)]
65. Wu, K.; Chen, J.; McBride, J.R.; Lian, T. Efficient Hot-Electron Transfer by a Plasmon-Induced Interfacial Charge-Transfer Transition. *Science* **2015**, *349*, 3584–3588. [[CrossRef](#)] [[PubMed](#)]
66. Okamoto, K.; Niki, I.; Shvartser, A.; Narukawa, Y.; Mukai, T.; Scherer, A. Surface-Plasmon-Enhanced Light Emitters Based on InGaN Quantum Wells. *Nat. Mater.* **2004**, *3*, 601–605. [[CrossRef](#)] [[PubMed](#)]
67. Naldoni, A.; Montini, T.; Malara, F.; Mróz, M.M.; Beltram, A.; Virgili, T.; Boldrini, C.L.; Marelli, M.; Romero-Ocaña, I.; Delgado, J.J.; et al. Hot Electron Collection on Brookite Nanorods Lateral Facets for Plasmon-Enhanced Water Oxidation. *ACS Catal.* **2017**, *7*, 1270–1278. [[CrossRef](#)]
68. Thimsen, E.; Le Formal, F.; Grätzel, M.; Warren, S.C. Influence of Plasmonic Au Nanoparticles on the Photoactivity of Fe₂O₃ Electrodes for Water Splitting. *Nano Lett.* **2011**, *11*, 35–43. [[CrossRef](#)] [[PubMed](#)]
69. Naphade, R.A.; Tathavadekar, M.; Jog, J.P.; Agarkar, S.; Ogale, S. Plasmonic Light Harvesting of Dye Sensitized Solar Cells by Au-Nanoparticle Loaded TiO₂ Nanofibers. *J. Mater. Chem. A* **2014**, *2*, 975–984. [[CrossRef](#)]
70. Movsesyan, A.; Marguet, S.; Muravitskaya, A.; Béal, J.; Adam, P.-M.; Baudrion, A.-L. Influence of the CTAB surfactant layer on optical properties of single metallic nanospheres. *J. Opt. Soc. Am. A* **2019**, *36*, C78. [[CrossRef](#)]
71. Thakur, M.K.; Gupta, A.; Fakhri, M.Y.; Chen, R.S.; Wu, C.T.; Lin, K.H.; Chattopadhyay, S. Optically coupled engineered upconversion nanoparticles and graphene for a high responsivity broadband photodetector. *Nanoscale* **2019**, *11*, 9716–9725. [[CrossRef](#)]

72. Elsharif, A.M. The Effect of the Electron Tunneling on the Photoelectric Hot Electrons Generation in Metallic-Semiconductor Nanostructures. *Chem. Phys. Lett.* **2018**, *691*, 224–230. [[CrossRef](#)]
73. Wiecha, P.R. pyGDM—A python toolkit for full-field electro-dynamical simulations and evolutionary optimization of nanostructures. *Comput. Phys. Commun.* **2018**, *233*, 167–192. [[CrossRef](#)]
74. Willingham, B.; Brandl, D.W.; Nordlander, P. Plasmon hybridization in nanorod dimers. *Appl. Phys. B Lasers Opt.* **2008**, *93*, 209–216. [[CrossRef](#)]
75. Kumarasinghe, C.S.; Premaratne, M.; Bao, Q.; Agrawal, G.P. Theoretical Analysis of Hot Electron Dynamics in Nanorods. *Sci. Rep.* **2015**, *5*, 12140. [[CrossRef](#)]
76. Wang, M.; Han, Y.; Liu, X.; Nie, Z.; Deng, C.; Guo, M.; Yao, S. Assembly of layer-by-layer films of superoxide dismutase and gold nanorods: A third generation biosensor for superoxide anion. *Sci. China Chem.* **2011**, *54*, 1284–1291. [[CrossRef](#)]